International Journal of Sciences

Research Article Volume 5 – November 2016 (11)

Study of Hybrid Microscopic and Macroscopic Buckling in UV Treated PDMS

Abbas Sabbah[1,2], Ayman Youssef[2], Pascal Damman[1]

[1]Interfaces and Complex Fluids Laboratory (INFLUX), Center of Innovation and Research in Materials and Polymers (CIRMAP), University of Mons (UMONS), Place du Parc 20, B-7000 Mons, Belgium; pascal.damman@umons.ac.be

[2]Lebanese University, Lebanon; ayman.youssef@ul.edu.lb

Abstract: Plant leaves, insect wings, and other natural surfaces show interesting cases of out-of-plan deformations, which can be attributed to mechanical buckling. This paper deals with a specific type of elastic instabilities, where both microscopic (wrinkles) and macroscopic (global curvature) deformations occur simultaneously. To this end, PDMS narrow sheet was stretched, its surface oxidized, then released. Its deformation was measured and analyzed. A mechanical model considering the effect of wrinkle on elasticity was elaborated; the concept equivalent stiffness was introduced in order to represent this effect. The model was matched with testing results successfully. This model is an interesting tool to explain potentially number of elastic instability phenomena.

Keywords: global buckling, stiff layer, microstructures, wrinkles, elastomers, equivalent stiffness

Introduction

Mechanical buckling instabilities might lead to out-of-plane deformation such as wrinkles, creasing, or other macroscopic shapes like cylindrical, spherical or saddle surfaces.

Such deformations can be seen in the nature like in the plant leaves; where several interesting works were done to analyze and understand; e.g. Jeong et al.[1] modeled leaves as two layers and studied their 3D deformation when drying, proposing numerical simulation methodes to this end. On the other hand, when these deformations occure in structure or in industrial process, they might cause performance degradation or induce mechanical failures.

Whilst engineers worked to eliminate such instabilities in the past, large number of researcher works demonstrate that this phenomenon can be useful if well studied, understood, and controlled.

Huang et al.[2] studied wrinkles in a layered structure, and performed simulations which confirmed analytical models. Diab et al.[3], [4] analyzed formation of wrinkles; but instead of multiple layers' structure, they used nonlinear neo-Hookean solid surface with its elastic stiffness decaying exponentially with depth. They found the compression strains at which bifurcation occurs using FEA. De Haan et al.[5] used the photopatterning of liquid crystals in order to control wrinkles pattern on metal (gold) surface, for applications ranging from diffractive elements to fine jewelry. Li et al.[6] used the wrinkles to induce stress paterns in elastic metamaterials with periodic microstructures in order to control wave propagation (filter) which can be used in accoustics, vibration control, etc.

While the above papers, among others, deal with wrinkles (microscopic buckling) and show some of their applications, other papers dealt with macroscopic buckling by studying, performing simulations and testing, and emphasinsing interesting applications. Huang et al.[7] studied prestrained elastomeric bilayer strips, where alternating helices were produced and analysed. Mora and Boudaoud[8]

Published at: http://www.ijsciences.com/pub/issue/2016-11/
DOI: 10.18483/ijSci.1149; Online ISSN: 2305-3925; Print ISSN: 2410-4477

Abbas Sabbah (Correspondence)
Abbas.Sabbah@gmail.com
+961-3-464969

studied the geometry thin swelling soft gel layer clamped to a stiff gel layer. McHall et al.[9] analyzed wrapping effect and used it to create desired three dimensional (3D) shapes from initially flat sheets using droplet. A method to produce temperature-responsive gel sheets was proposed by Kim et al.[10]; these sheets can take, under temperature effect three-dimensional shape, predefined by the map of irradiation dose. Another interesting application of buckling by prestretching is proposed by Maji et al.[11]; fully flexible electronics and sensors for conformal integration applications.

When a flat piece of cross-linked and cured PDMS is stretched and then oxidized, a stiff thin layer is formed on its surface, so that when it is released, elastic instabilities occur. Depending on the parameters of the experiment, the elastic instabilities can be microscopic (wrinkles) and/or macroscopic (global buckling); moreover, global buckling can be either uniaxial or biaxial.

In contrast with previous works where either microscopic or macroscopic instabilities where studied, this paper emphasizes hybrid buckling case where both microscopic and macroscopic buckling appear simultaneously, focusing mainly on uniaxial deformation. The final geometry of the sample changes depending on compression ratio, while the other parameters were fixed.

The analysis of results aimed to understand and to model the final geometry (radius of curvature) in terms of compression ratio. It starts with the simplest possible model, i.e. pure geometric. Then it was approached from mechanical point of view (Force and Moment Equilibrium). Model 1 considered a first assumption that the stiff layer is incompressible. Model 2 is more elaborated with the introduction of equivalent stiffness notion.

Materials and Methods

Experiments were carried out using polydimethylsiloxane (PDMS) elastomer (Sylgard 186) obtained from Dow Corning (Midland, MI, United States). It is supplied as a two-part kit: a liquid silicone rubber base and a catalyst or curing agent. The substrates are prepared by mixing a ratio 10:1 (base: curing agent), defoaming for 30 minutes and cross-linking at 75°C temperature for two hours. The Young's modulus, measured with a Mettler Toledo Dynamic Mechanical Analysis (DMA) 861e, is estimated around 1 MPa for Sylgard 186.

After cross-linking, the two ends of PDMS (Sylgard 186) sample were clamped to the fixed and moving parts of hand wheel precise sliding table module, the sample being at rest (no internal stress). The distance between the clamps is measured, note L.

The moving end of the sliding table was moved in order to stretch the PDMS sample. The distance between the clamps is increased to L_0. (Figure 1, i).

The upper face of stretched PDMS sample is oxidized using Ultra Violet Ozone UV/O_3 (Applitek PR100, Nazareth, Belgium) (Figure 1, ii). The UV/O_3 treatment changes the surface chemistry of PDMS. It converts it into a silicate based stiff layer (SiO_x); the thickness of the stiff skin layer (top layer) increases with irradiation time[12]–[14]. After the UV/O_3 treatment for a defined period of time, the silicate thin rigid layer is formed on top of the thick soft elastomeric substrate.

The stretching is finally relaxed, so that the substrate layer is compressing the top layer (Figure 1, iii). The compression ratio is defined by:

$$\delta = \frac{L_0 - L}{L_0} \qquad (1)$$

Above some threshold for the compression ratio ($\delta > \delta_c$), we observe the formation of sinusoidal

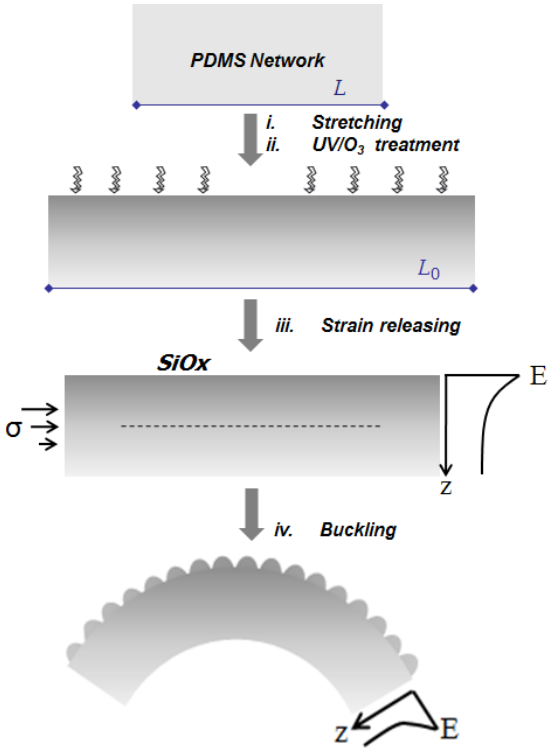

Figure 1 (i) Stretching from L to L_0 (ii) UV/O3 treatment while stretched (iii) graphical representations of gradient elastic modulus and compression stress (iv) Structure after compression.

wrinkles on the top of the PDMS characterized by a cylindrical symmetry and oriented perpendicular to the direction of maximum stress; for short exposure time, the sample remains flat [12], [15], [16]. In this study, we extended the exposure time UV/O_3 to three hours (180 mins); this procedure leads to macroscopic buckling (global undulation) too (Figure 1, iv).

In the case of wide samples, the macroscopic buckling can appear in in two directions (biaxial). In this paper, we are interested in uniaxial buckling (one direction). To this end, we stretched a slim film of PDMS (L = 3.5cm, l = 0.6cm and H = 1.5mm) uniaxially, then treated for 3 hours at the UV/O_3. We varied the stretch ratio of PDMS from 20% to 220% (Figure 2).

The measurements were performed from macro photography of the cross-section of the samples.

Results and Discussion

This UV/O_3 treatment particularly long leads to an increase of the thickness of the silica layer. The stiff silica surface will keep its shape and PDMS wants to return to its original position. The result of this competition leads to a macroscopic deformation. Figure 2 summarizes the results for different compression ratios. In an interesting way, a decrease in the bending radius is observed with increasing the compression ratio.

Figure 2 PDMS 186 Sample treated for 3 hours at the UV/O_3 and then compressed at different rates (20% - 220%).

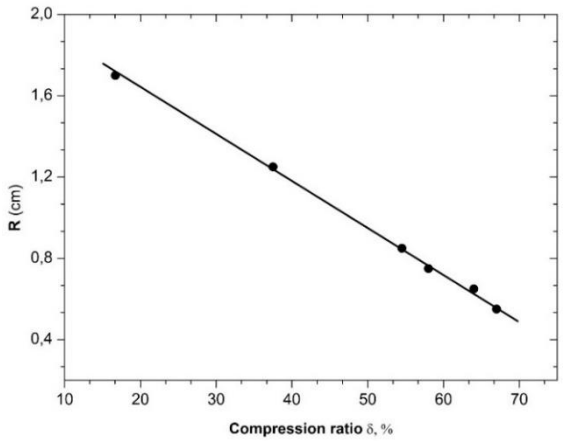

Figure 3. Plot of curvature radius representing the decrease of radius in function of the stress.

The graph in Figure 3 shows the variation of the inner radius versus the compression ratio.

Based on a purely geometric approach, we can show that the bending radius should evolve according to a simple law $R_o = t / 2\delta$, where t denotes the thickness of the PDMS film. The graph in Figure 3 shows that the radius follows this trend, but does not reproduce accurately the geometric model. For this reason, it was decided to consider mechanical stresses in the model.

In the following subsections a model based on stress analysis (equilibrium of force and moment) is developed. A first attempt was based on the assumption that the thin stiff layer is rigid (constant length). The model is then improved by introducing the notion of equivalent stiffness.

Force and Moment Equilibrium

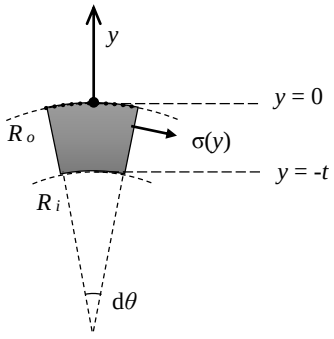

Figure 4. Partial cross section of the PDMS after elastic deformation

Figure 4 shows a macroscopic view of the PDMS after being bent. We define the ordinate y in the radial direction so that at any point:

$$R = R_o + y \tag{1}$$

The difference between R_o the outer radius and R_i the inner radius is *t*, the actual thickness of the PDMS:

$$t = R_o - R_i \tag{2}$$

In order to analyze the stress and the strain in the PDMS, we choose a section which is orthogonal to the macroscopic deformation line. The neutral line is the line where the normal stress σ and the strain ε (in tangential direction) vanish.

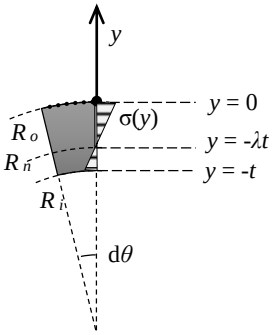

Figure 5. Normal stress distribution on PDMS section

We assume that it is located at $y = -\lambda t$; the corresponding radius is R_n and the corresponding length is L, which is the initial length of PDMS, before stretching.

$$\lambda t = R_o - R_n \tag{3}$$

The following equations can be concluded from the geometry:

$$\Delta\theta = \frac{L_o}{R_o} = \frac{L_i}{R_i} = \frac{L}{R_n} = \frac{L(y)}{R_o + y} \tag{4}$$

A simple mathematical manipulation leads to the following:

$$\Delta\theta = \frac{L(y) - L}{R_o + y - R_n} = \frac{L_o - L}{R_o - R_n} \tag{5}$$

Replacing equation (3) in the above:

$$\Delta\theta = \frac{L(y) - L}{\lambda t + y} = \frac{L_o - L}{\lambda t} \tag{6}$$

The strain at a given ordinate y, where the arc length is $L(y)$ is:

$$\varepsilon = \frac{L(y) - L}{L} = \frac{L_o - L}{L\lambda t}(\lambda t + y) \tag{7}$$

Therefore, the stress is:

$$\sigma(y) = E_P\varepsilon = E_P\frac{L_o - L}{L\lambda t}(\lambda t + y) = A(\lambda t + y) \tag{8}$$

Where we defined the constant:

$$A \overset{\text{def}}{=} E_P\frac{L_o - L}{L\lambda t} \tag{9}$$

The equilibrium equations for the section as shown in Figure 5 are the following:

$$\text{Force: } \int_{-t}^{0}\sigma(y)dy = F_{CL}$$

$$\text{Moment: } \int_{-t}^{0}\sigma(y)ydy = F_{CL} \times 0 = 0$$

where the force F_{CL} is transferred from the stiff layer to the PDMS, per unit of length and depth. We assume that this force is applied on the outer radius ($y = 0$), and thus it has no moment around the origin.

Moment:

$$0 = A\left(-\frac{1}{2}\lambda + \frac{1}{3}\right)t^3$$

Thus

$$\lambda = \frac{2}{3} \tag{10}$$

Force:

$$F_{CL} = A\left(\lambda - \frac{1}{2}\right)t^2 = \frac{At^2}{6}$$

Therefore:

$$F_{CL} = E_P\frac{L_o - L}{4L}t \tag{11}$$

Model 1: Rigid Stiff Layer

We assume in this model that the stiff layer is infinitely stiff, and thus the curing length (after stretching), noted L_C , which is the initial length of stiff layer, is kept unchanged.

Therefore, the equation $L_o = L_C$ determines the final geometry.

Equations (4) and (6) yields to:

$$\frac{R_o}{L_o} = \frac{\lambda t}{L_o - L} \qquad (12)$$

Thus,

$$R_o = \frac{\lambda t L_o}{L_o - L} \qquad (13)$$

Replacing by $\lambda = \frac{2}{3}$, and $L_o = L_C$:

$$R_o = \frac{2}{3}\frac{tL_C}{L_C - L} = \frac{2}{3}\frac{t}{\delta} \qquad (14)$$

where $\delta \overset{\text{def}}{=} \frac{L_C - L}{L_C}$ denotes the compression ratio.

The equation (14) representing the "model 1" is plotted in Figure 6, simultaneously with the measured radii.

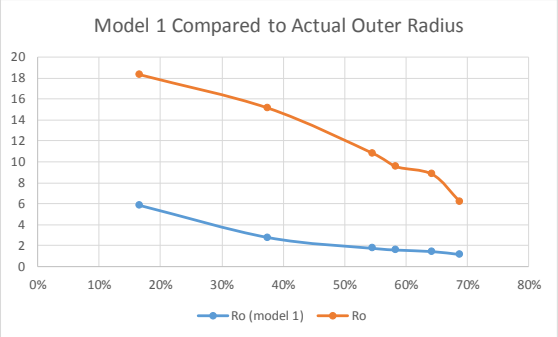

Figure 6. Experimental results compared to model 1: Outer radius versus compression ratio

It's obvious that model 1 shows lower radius values (stronger curvature) compared to real case, which means that the assumption of ultimately stiff layer is not realistic; the stiff layer should have additional flexibility, and this flexibility is assured by the means of wrinkles.

Model 2: Equivalent Stiffness after Buckling

Before buckling, the force reaction to compression of the stiff layer, note F_C, is directly proportional to its section, and to its Young's modulus E_F:

$$F_C = K_S \frac{\Delta L}{L_C} \quad \text{with} \quad K_S = E_F \times h_F \times b \qquad (15)$$

L_C is the initial length of the stiff layer, h_F its thickness, b the width of the sample.

After buckling, its force reaction is drastically reduced due to elastic instability; we introduced here the notion of equivalent stiffness of the stiff layer after buckling, note K_E;

$$F_C = K_E \frac{\Delta L}{L_C} \quad \text{where} \quad K_E \ll K_S \qquad (16)$$

This concept is similar to the helical spring, where the stiffness depends on the shape of the spring, in addition to its physical properties.

The reduced stiffness becomes comparable to the stiffness of PDMS, therefore, we shall consider that the stiff layer is compressed to the final length L_o, lesser than L_C, and determined by the equilibrium of forces.

The force transferred per unit of width is:

$$F_{CL} = \frac{F_C}{b} = \frac{K_E \Delta L}{L_C b} = K\frac{\Delta L}{L_C}$$

Thus

$$F_{CL} = K\frac{L_C - L_o}{L_C} \qquad (17)$$

Where K is defined as:

$$K \overset{\text{def}}{=} \frac{K_E}{b} \qquad (18)$$

Comparing equations (11) and (17):

$$K\frac{L_C - L_o}{L_C} = E_P \frac{L_o - L}{4L} t \qquad (19)$$

Knowing that $\delta \overset{\text{def}}{=} \frac{L_C - L}{L_C}$, the value of $L = (1-\delta)L_C$ can be replaced in the equation above:

$$K\frac{L_C - L_o}{L_C} = E_P \frac{L_o - (1-\delta)L_C}{4(1-\delta)L_C} t$$

Therefore:

$$4(1-\delta)\frac{K}{tE_P}(L_C - L_o) = L_o - (1-\delta)L_C$$

After some manipulations, the equilibrium length is concluded:

$$L_o = \frac{tE_P + 4K}{tE_P + 4K(1-\delta)}(1-\delta)L_C = \frac{tE_P + 4K}{tE_P + 4K(1-\delta)}L \qquad (20)$$

The equivalent outer radius is obtained from equation (13):

$$R_o = \frac{2}{3}t\frac{L_o}{L_o - L} \qquad (21)$$

Replacing R_o by its value from (20):

$$R_o = \frac{tE_P + 4K}{6K\delta}t \qquad (22)$$

Therefore

$$\frac{6\delta R_o}{t} = \frac{tE_P + 4K}{K} \qquad (23)$$

Thus:

$$\frac{K}{E_P} = \frac{t^2}{6\delta R_o - 4t} \qquad (24)$$

Where R_o and t are measured (in mm), δ is dimensionless, E_p is expressed in MPa and K in N/mm.

When $\frac{K}{E_P}$ is plotted versus $\delta \overset{\text{def}}{=} \frac{L_C - L}{L_C}$ (Figure 7), it is obvious that it is decreasing when δ is low, then it becomes almost constant for higher δ values.

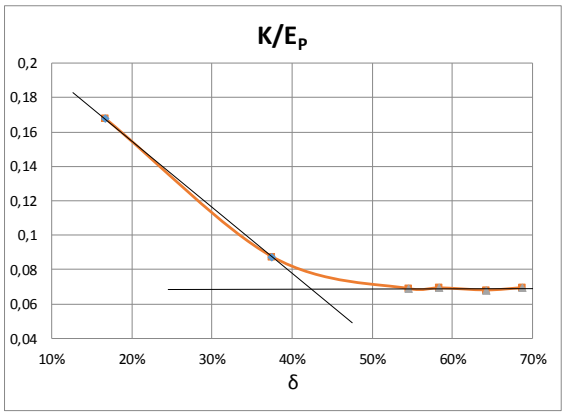

Figure 7. Plot of K/E_P versus δ (orange) and trend lines for low and for high δ values (black)

In order to explain this change, the behavior of the wrinkles should be observed for different compression rates.

However, the actual compression rate at the wrinkles level is related to the curing length L_C (initial) and the equilibrium length L_o. Note δ' this compression rate, it is defined as:

$$\delta' \overset{\text{def}}{=} \frac{L_C - L_o}{L_C} \qquad (25)$$

In Figure 8, $\frac{K}{E_P}$ is plotted against the actual compression rate δ'.

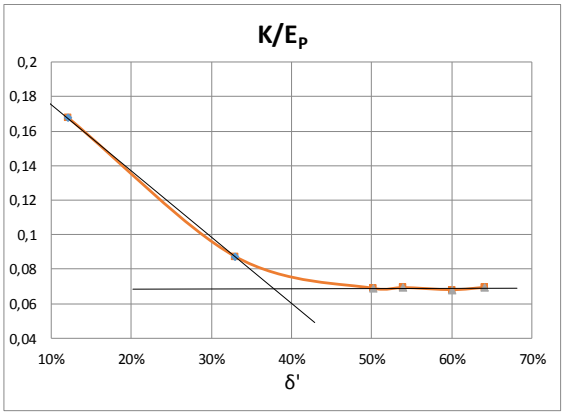

Figure 8. Plot of K/E_P versus δ' (orange) and trend lines for low and for high δ' values (black)

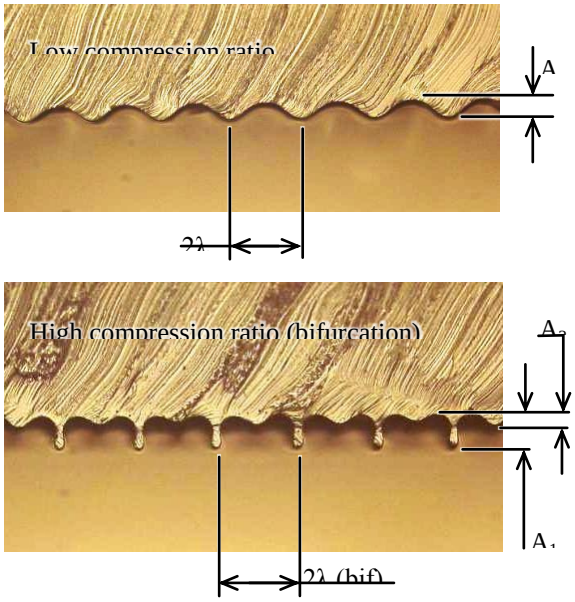

Figure 9. Shape of the wrinkles section cuts, as observed by optical microscope, at different compression rates.

At low rates (Figure 9, upper), the wrinkles keep sinewave shape; where Figure 10 shows that the amplitude is increasing (upper plot), whilst the wavelength decrease with the compression rate (lower plot).

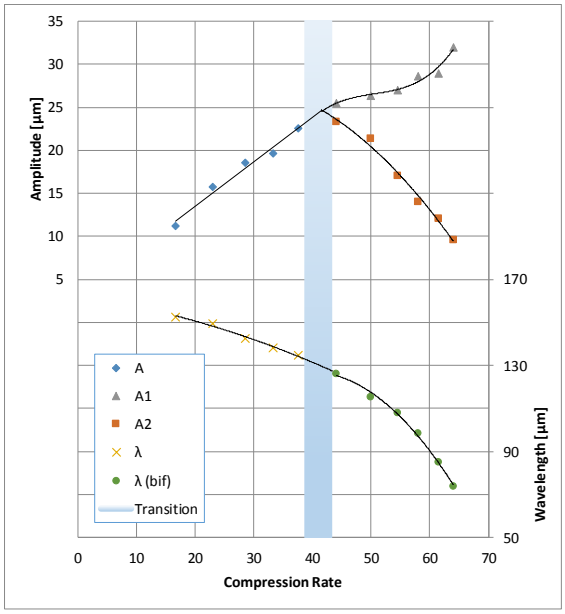

Figure 10. Plots of wrinkle amplitude and wavelength versus compression rate[17], *i.e. δ'*

Noting that the equivalent stiffness of wrinkles layer is decreasing with amplitude and increasing with wavelength[17], one can explain the first segment of Figure 8 where the equivalent stiffness function $\frac{K}{E_P}$ is decreasing.

After the bifurcation, at high ratio (Figure 9, lower), the structure of the wrinkles is frozen; therefore, the value of equivalent stiffness is fixed, which explains the second segment of the graph in Figure 8.

Conclusion

The authors of this paper studied elastic instabilities occurring in PDMS with oxidized stiff layer. They focused on hybrid uniaxial deformation, where both wrinkles and global buckling appeared simultaneously.

The variation of radius of curvature in terms of compression ratio was analyzed and verified to be decreasing.

It was shown that a pure geometric model cannot explain the experimental results.

At this point, the authors studied it from mechanical point of view (Force and Moment Equilibrium). Model 1 considered a first assumption that the stiff layer is incompressible. The results of this model do not comply with experimental results.

This discrepancy is attributed to the fact that the microscopic instabilities (wrinkles) decrease drastically the actual stiffness of the stiff layer.

There was the main motivation to introduce the notion of equivalent stiffness, leading to Model 2. The experimental results confirmed model 2, where the stiffness function became constant when the wrinkle structure was frozen (post-bifurcation).

Abbreviations

The following abbreviations are used in this manuscript:

PDMS: poly-dimethylsiloxane

UV/O_3: Ultra Violet Ozone

FEA: finite element analysis

3D: Three dimensional

DMA: Dynamic Mechanical Analysis

References

[1] S. Jeong, S. H. Park, and C. H. Kim, "Simulation of morphology changes in drying leaves," *Comput. Graph. Forum*, vol. 32, no. 1, pp. 204–215, 2013.

[2] Z. Y. Huang, W. Hong, and Z. Suo, "Nonlinear analyses of wrinkles in a film bonded to a compliant substrate," *J. Mech. Phys. Solids*, vol. 53, no. 9, pp. 2101–2118, 2005.

[3] M. Diab, T. Zhang, R. Zhao, H. Gao, and K.-S. Kim, "Ruga mechanics of creasing: from instantaneous to setback creases," *Proc. R. Soc. A Math. Phys. Eng. Sci.*, vol. 469, no. 2157, pp. 20120753–20120753, 2013.

[4] M. Diab and K.-S. Kim, "Ruga-formation instabilities of a graded stiffness boundary layer in a neo-Hookean solid," *Proc. R. Soc. A Math. Phys. Eng. Sci.*, vol. 470, pp. 20140218–20140218, 2014.

[5] L. T. De Haan, P. Leclère, P. Damman, A. P. H. J. Schenning, and M. G. Debije, "On-demand wrinkling patterns in thin metal films generated from self-assembling liquid crystals," *Adv. Funct. Mater.*, vol. 25, no. 9, pp. 1360–1365, 2015.

[6] G.-Y. Li, Y. Zheng, Y.-P. Cao, X.-Q. Feng, and W. Zhang, "Controlling elastic wave propagation in a soft bilayer system via wrinkling-induced stress patterns," *Soft Matter*, vol. 12, pp. 4204–4213, 2016.

[7] J. Huang, J. Liu, B. Kroll, K. Bertoldi, and D. R. Clarke, "Spontaneous and deterministic three-dimensional curling of pre-strained elastomeric bi-strips," *Soft Matter*, vol. 8, no. 23, p. 6291, 2012.

[8] T. Mora and A. Boudaoud, "Buckling of swelling gels," *Eur. Phys. J. E*, vol. 20, no. 2, pp. 119–124, 2006.

[9] G. McHale, M. I. Newton, N. J. Shirtcliffe, and N. R. Geraldi, "Capillary origami: Superhydrophobic ribbon surfaces and liquid marbles," *Beilstein J. Nanotechnol.*, vol. 2, no. 1, pp. 145–151, 2011.

[10] J. Kim, J. a. Hanna, M. Byun, C. D. Santangelo, and R. C. Hayward, "Designing Responsive Buckled Surfaces by Halftone Gel Lithography," *Science (80-.).*, vol. 335, no. 6073, pp. 1201–

1205, 2012.

[11] D. Maji, D. Das, J. Wala, and S. Das, "Buckling assisted and lithographically micropatterned fully flexible sensors for conformal integration applications," *Nat. Publ. Gr.*, no. August, pp. 1–8, 2015.

[12] V. Roucoules, A. Ponche, A. Geissler, F. Siffer, L. Vidal, S. Ollivier, M. F. Vallat, P. Marie, J. C. Voegel, P. Schaaf, and J. Hemmerlé, "Changes in silicon elastomeric surface properties under stretching induced by three surface treatments," *Langmuir*, vol. 23, no. 26, pp. 13136–13145, 2007.

[13] K. Efimenko, W. E. Wallace, and J. Genzer, "Surface Modification of Sylgard-184 Poly(dimethyl siloxane) Networks by Ultraviolet and Ultraviolet/Ozone Treatment," *J. Colloid Interface Sci.*, vol. 254, no. 2, pp. 306–315, 2002.

[14] Y. J. Fu, H. Z. Qui, K. S. Liao, S. J. Lue, C. C. Hu, K. R. Lee, and J. Y. Lai, "Effect of UV-Ozone treatment on poly(dimethylsiloxane) membranes: Surface characterization and gas separation performance," *Langmuir*, vol. 26, no. 6, pp. 4392–4399, 2010.

[15] K. Efimenko, M. Rackaitis, E. Manias, A. Vaziri, L. Mahadevan, and J. Genzer, "Nested self-similar wrinkling patterns in skins.," *Nat. Mater.*, vol. 4, no. 4, pp. 293–7, 2005.

[16] A. Sabbah, A. Youssef, and P. Damman, "Superhydrophobic Surfaces Created by Elastic Instability of PDMS," *Appl. Sci.*, vol. 6, no. 5, p. 152, 2016.

[17] F. Brau, H. Vandeparre, A. Sabbah, C. Poulard, A. Boudaoud, and P. Damman, "Multiple-length-scale elastic instability mimics parametric resonance of nonlinear oscillators," *Nat. Phys.*, vol. 7, no. 1, pp. 56–60, 2010.